Journal of Materials Chemistry A

ROYAL SOCIETY OF CHEMISTRY

PAPER

Published on 04 August 2026

Cite this: DOI: 10.1039/d6ta05412a

Methanol-mediated turbostratic activation of CoAl-LDHs for high-efficiency fluoride capture: a solvent-exclusion mechanism

Chaoyao Yao,[a] Jinan Niu, *[ab] Mingge Zhi,[a] Ruixuan Zhang,[a] Shunle Zhou,[a] Sonehra Anjum,[a] Fangfang Liu,[a] Arianit A. Reka,[c] Farid Akhtar, [d] Peizhong Feng*[ab] and Hermenegildo Garcia *[e]

Carbonate intercalation in layered double hydroxides (LDHs) strongly restricts interlayer accessibility and limits their fluoride capture performance under near-neutral conditions. Herein, we report a methanol–nitric acid activation strategy to regulate the interlayer chemistry and stacking structure of mechanochemically synthesized CoAl-LDHs. The treatment partially replaced interlayer carbonate with nitrate/methanol-associated species, expanded the basal spacing, and increased turbostratic disorder while preserving the Co–Al hydroxide host-layer framework and a stable Co/Al ratio. Under neutral conditions, the optimized Co_3Al_2-MN-LDH achieved 94.89% fluoride removal at an initial F^- concentration of 10 mg L^{-1}, an adsorbent dosage of 0.5 g L^{-1}, and an initial pH of 7.0, corresponding to a nearly four-fold enhancement over the pristine water-washed LDH. Post-adsorption XRD, FTIR, and XPS analyses indicate that fluoride uptake involves partial anion exchange, exclusion of methanol-related interlayer species, and local electronic adjustment of the metal hydroxide layers, rather than dissolution–reprecipitation of the LDH framework. Kinetic analysis showed that fluoride adsorption was better described by the pseudo-second-order model, with film diffusion contributing to the initial stage, while thermodynamic analysis suggested a favorable adsorption process with a positive entropy contribution. This work highlights solvent-assisted interlayer activation as an effective route for improving fluoride capture by mechanochemical LDHs in neutral fluoride-containing aqueous systems, particularly industrial fluoride-bearing streams.

Received 27th June 2026
Accepted 3rd August 2026

DOI: 10.1039/d6ta05412a

rsc.li/materials-a

1 Introduction

Fluoride (F^-)-containing aqueous streams constitute an important environmental and technological challenge in a wide range of industrial processes, including semiconductor manufacturing, electroplating, rare-earth processing, glass and ceramics production, coal-related industries, and phosphate fertilizer production. In these systems, excessive fluoride may cause equipment corrosion, process instability, catalyst deactivation, and difficulties in meeting discharge requirements. Meanwhile, fluoride contamination in natural waters remains a long-standing environmental issue, especially in regions such as the East African Rift Valley, Northern China, and India.[1] Excessive fluoride levels in aqueous systems can lead not only to severe human health risks[2] but also to corrosion, process instability, catalyst deactivation, and discharge compliance issues in industrial operations. Among available remediation technologies, adsorption remains one of the most practical approaches owing to its operational simplicity, economic feasibility, and adaptability to diverse water matrices.[3]

Layered double hydroxides (LDHs), also known as anionic clays, are attractive fluoride adsorbents because of their positively charged hydroxide layers, tunable composition, and intrinsically high anion-exchange capacity.[4–7] However, their adsorption performance is frequently limited by the strong affinity of carbonate ions toward the LDH interlayer. Carbonate ions possess high charge density and form stable interactions with the metal hydroxide layers, leading to compact interlayer stacking and restricted accessibility of internal adsorption sites.[8] Consequently, carbonate-intercalated LDHs often display relatively limited fluoride uptake under near-neutral conditions.[9]

To improve interlayer accessibility, various decarbonation and anion-exchange approaches have been explored, including calcination–reconstruction,[10,11] aqueous acid/salt treatment,[12,13]

[a]Mineral-based Energy and Environmental Materials Laboratory (ME^2 Lab), School of Materials Science and Physics, China University of Mining and Technology, Xuzhou, 221116, China. E-mail: jinan.niu@cumt.edu.cn; pzfeng@cumt.edu.cn

[b]Jiangsu Key Laboratory for Clean Utilization of Carbon Resources, China University of Mining and Technology, Xuzhou, 221116, China

[c]Faculty of Natural Sciences and Mathematics, University of Tetova, Tetovo, 1200, North Macedonia

[d]Division of Materials Science, Luleå University of Technology, Luleå, 97187, Sweden

[e]Instituto de Tecnologia Quimica CSIC-UPV, Universitat Politecnica de Valencia, Valencia, 46022, Spain. E-mail: hgarcia@qim.upv.es

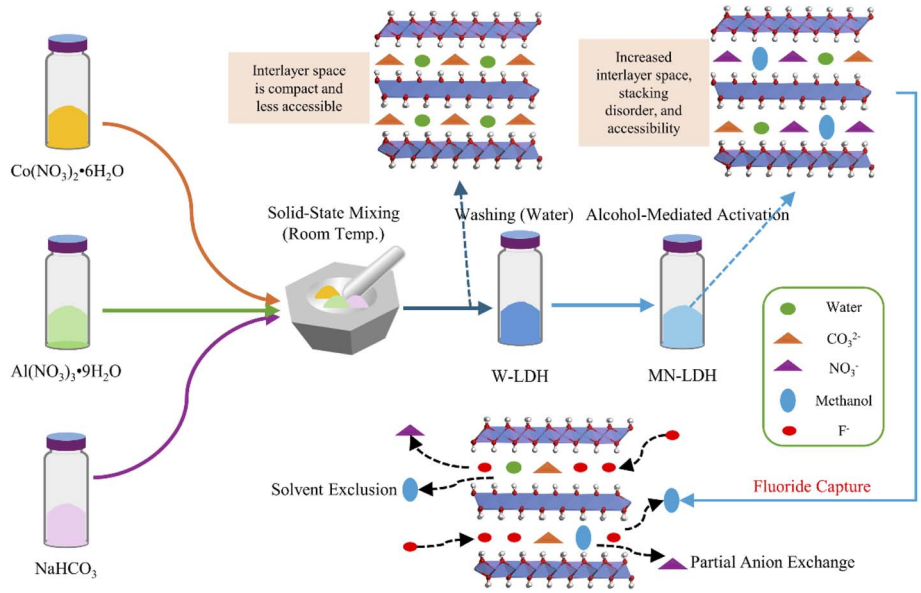

Fig. 1 Schematic illustration of methanol-assisted activation and solvent-exclusion-assisted fluoride capture by CoAl-LDHs.

and solvent-assisted exchange strategies.[14–16] Alcohol-mediated treatments are of particular interest because reducing the dielectric constant of the exchange medium can facilitate interlayer ion replacement while mitigating extensive layer dissolution. Previous studies, including the alcohol-mediated ordered stacking transformation (AMOST) strategy for LDHs, have demonstrated that solvent environments can strongly influence LDH stacking characteristics and interlayer chemistry.

Nevertheless, most existing studies focus on well-crystallized hydrothermal or commercial LDHs and primarily seek to preserve or optimize structural order during exchange processes. Comparatively little attention has been devoted to solvent-mediated modification of as-synthesized mechanochemical LDH precursors. Such materials often exhibit distinct defect distributions, aggregation states, and metastable structural characteristics that may respond differently to solvent treatment than conventionally synthesized LDHs. Understanding how solvent environments regulate interlayer chemistry and stacking characteristics in mechanochemical LDHs may therefore provide new opportunities for tuning adsorption behavior.

From an application perspective, fluoride removal under near-neutral conditions is highly relevant to both natural waters and industrial process streams. Therefore, adsorption experiments in this study were deliberately conducted at an initial pH of 7.0 to evaluate material performance under environmentally and technologically relevant conditions.

Herein, we report a methanol-mediated activation strategy for mechanochemically synthesized CoAl-LDHs (Fig. 1). By combining methanol treatment with nitrate-assisted interlayer modification, the initially carbonate-dominated LDH precursor is transformed into a more accessible phase with altered stacking characteristics and interlayer chemistry. Through structural characterization and adsorption thermodynamic analysis, we investigate how solvent-mediated regulation influences fluoride capture behavior and discuss a solvent-exclusion mechanism associated with methanol-containing interlayer environments. This work provides insight into solvent-controlled regulation of mechanochemical LDHs for fluoride capture in neutral aqueous systems.

2 Experimental

2.1 Materials and methods

Cobalt nitrate hexahydrate ($Co(NO_3)_2 \cdot 6H_2O$), aluminum nitrate nonahydrate ($Al(NO_3)_3 \cdot 9H_2O$), sodium bicarbonate ($NaHCO_3$), and nitric acid (1 mol L^{-1}) were all of analytical grade (AR), purchased from Sinopharm Chemical Reagent Co., Ltd (Shanghai), and used as received without further purification.

2.1.1 Synthesis of pristine LDH *via* mechanochemical method. Aluminum nitrate and cobalt nitrate were weighed according to specific molar ratios (3 : 2, 2 : 1, 3 : 1, and 4 : 1). Sodium bicarbonate was added at a ratio of 3 : 1 to the total amount of metal salts. The mixture was ground in a mortar at room temperature for 30 min. The resulting product was washed with deionized water, followed by centrifugation at 8000 rpm for 3 min. The final product, designated as W-LDH (water-washed LDH), was obtained after drying at 60 °C.

2.1.2 Preparation of activated LDH *via* alcohol-mediated exchange. To obtain the activated samples, 0.1 g of W-LDH was dispersed in 45 mL of absolute methanol and ultrasonicated for 5 min to form a uniform suspension. The suspension was then vigorously stirred under a nitrogen atmosphere. Simultaneously, 5 mL of a methanol–nitric acid mixed solution was added dropwise (over approximately 1 min). The dosage of HNO_3 was calculated to be twice the molar equivalent of the CO_3^{2-} (for instance, for Co_3Al_2-LDH, 0.396 mL of nitric acid was diluted to 5 mL with methanol). After stirring for 30 min, the product was washed with methanol, centrifuged,

and vacuum-dried at 60 °C to yield MN-LDH (methanol–nitric acid treated LDH).

For comparative studies on the structural evolution during the exchange process, EN-LDH (ethanol–nitric acid treated) and WN-LDH (water–nitric acid treated) were also prepared by replacing methanol with an equal volume of ethanol or deionized water, respectively, while maintaining all other experimental parameters constant. Based on this, the sample after MN-LDH adsorbed fluoride ions was named MNF-LDH.

In the naming convention for LDHs, when it's necessary to distinguish between different Co/Al ratios, the Co and Al feed ratio is added before the name, such as Co_4Al-W-LDH, Co_3Al-WN-LDH, *etc.* However, in general discussions, the focus is on the optimal feed ratio (3 : 2), and the Co/Al ratio is no longer included. Instead, the treatment method is simply added before LDH, such as W-LDH, MN-LDH, EN-LDH, WN-LDH, and MNF-LDH.

2.2 Characterization

Crystalline phases of the synthesized materials were characterized using a Bruker D8 Advance X-ray diffractometer (AXS, Germany) equipped with Cu Kα radiation. The measurements were performed at an operating voltage of 40 kV and a current of 30 mA, covering a 2θ range of 5° to 80° with a scanning rate of 5° min^{-1}. Surface functional groups were identified *via* Fourier-transform infrared spectroscopy (FTIR, Bruker Tensor 27) using the KBr pellet technique within the wavenumber range of 400–4000 cm^{-1}. The surface elemental compositions and valence states were probed by X-ray photoelectron spectroscopy (XPS) on a Thermo Fisher ESCALAB 250XI system. Furthermore, the textural properties, including specific surface area and pore size distribution, were determined through N_2 adsorption–desorption isotherms at 77 K using a Micromeritics ASAP 2020 PLUS HD88 analyzer.

2.3 Fluoride removal tests

Fluoride-containing wastewater was simulated using NaF aqueous solutions. The concentration of fluoride ions was determined with a PXSJ-216F fluoride ion meter (Leici, Shanghai). Prior to measurement, a linear calibration curve was established using standard fluoride solutions ranging from 5 to 100 mg L^{-1}. Batch adsorption tests were performed by introducing a specified mass of adsorbent into 20 mL of the fluoride solution. The mixture was then agitated at a constant frequency for 6 hours in a thermostatic shaker to ensure adsorption equilibrium at the target temperature. Following phase separation *via* centrifugation, the residual fluoride concentration in the supernatant was quantified. To investigate the effect of initial pH, NaOH and HCl were employed for pH regulation. Competitive adsorption experiments were conducted using 10 mg L^{-1} fluoride solutions in the presence of SO_4^{2-}, Cl^-, HCO_3^- and PO_4^{3-} at concentrations of 5, 10, and 20 mg L^{-1}, respectively. The removal efficiency (R%) was calculated according to eqn (1):

$$R = \frac{C_0 - C_e}{C_0} \quad (1)$$

where C_0 and C_e are the initial concentration of fluoride solution and the concentration at adsorption equilibrium, respectively, in mg L^{-1}.

The fluoride ion adsorption capacity q at time t is calculated according to eqn (2):

$$q = \frac{(C_0 - C_t)V}{W} \quad (2)$$

where C_t is the concentration of the fluorine solution at time t, in mg L; V is the volume of the fluorine solution, in L; W is the mass of the adsorbent added, in g. The equilibrium adsorption capacity q_e is the adsorption capacity when C_t is the concentration of fluoride ions in the solution at adsorption equilibrium.

To evaluate the stability of the LDH host layers during fluoride capture, metal leaching was analyzed by inductively coupled plasma optical emission spectroscopy (ICP-OES, Agilent 5110). After fluoride adsorption under the optimized conditions (initial F^- concentration = 10 mg L^{-1}, adsorbent dosage = 0.5 g L^{-1}, initial pH = 7.0, contact time = 6 h), the suspension was centrifuged and the supernatant was collected. The aqueous phase was then passed through a 0.22 μm membrane filter to remove residual solid particles, acidified with dilute HNO_3, and analyzed by ICP-OES to determine the concentrations of dissolved Co and Al. These dissolved metal concentrations were used as indicators of possible host-layer dissolution or metal leaching during adsorption.

3 Results and discussion

3.1 Mechanochemical formation and methanol-assisted structural activation of CoAl-LDHs

The structural evolution of CoAl-LDHs during mechanochemical synthesis and subsequent methanol–nitric acid treatment was first examined by XRD (Fig. 2). During the grinding of cobalt/aluminum nitrates with $NaHCO_3$, visible effervescence was observed and gradually disappeared within approximately 10 min, indicating a rapid acid–base/metathesis reaction accompanied by CO_2 release. This mechanochemical process promotes hydrolysis–condensation of metal species and the formation of Co–Al hydroxide precursors under liquid-assisted grinding conditions. The overall reaction can be approximately represented by the following equation taking Co/Al = 3 : 2 as an example.

$$3Co(NO_3)_2\cdot 6H_2O + 2Al(NO_3)_3\cdot 9H_2O + 12NaHCO_3 \rightarrow [Co_3Al_2(OH)_{10}]CO_3\cdot nH_2O + 12NaNO_3 + 11CO_2\uparrow + mH_2O$$

Before water washing, the XRD patterns of the ground products were dominated by the sharp reflections of crystalline $NaNO_3$, residual $NaHCO_3$, and Na_2CO_3, whereas no clear Co- or Al-containing crystalline phase was detected (Fig. 2a). This result suggests that the Co–Al hydroxide species formed during grinding were present mainly as amorphous or poorly crystallized precursors, whose weak diffraction signals were masked by the highly crystalline salt matrix.[17,18]

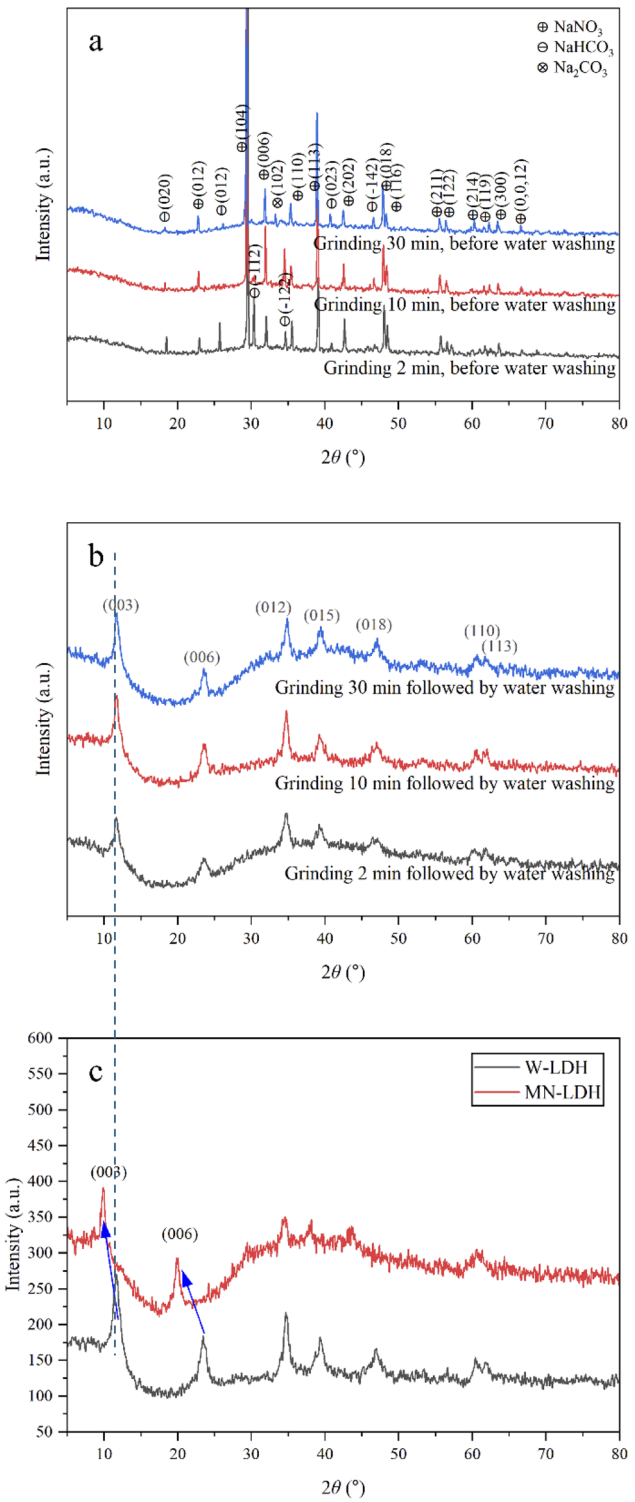

Fig. 2 XRD changes of products (a) before and (b) after water washing at different grinding times of raw materials at a Co/Al feed ratio of 3 : 2, and (c) before (W-LDH) and after (MN-LDH) methanol–nitric acid treatment. Note that the sample ground for 30 minutes in (b) is also shown in (c) to more clearly demonstrate the effect of interlayer species replacement on interlayer spacing.

After water washing, typical LDH reflections appeared at 11.7°, 23.5°, 34.8°, 39.4°, 60.6°, and 61.7°, corresponding to the (003), (006), (012), (015), (110), and (113) planes, respectively[19] (Fig. 2b). This confirms the formation of carbonate-intercalated CoAl-LDH after removal of the soluble salt byproducts. The intensity of the basal (003) reflection increased markedly when the grinding time was extended from 2 to 10 min, whereas further extension to 30 min produced no obvious improvement. These results indicate that the mechanochemical formation of CoAl-LDH is essentially completed within 10 min under the present conditions, although 30 min grinding was used in the following experiments to ensure complete precursor conversion.

The effect of methanol–nitric acid treatment on the water-washed LDH was then evaluated (Fig. 2c). Compared with W-LDH, MN-LDH showed an obvious shift of the basal (003) and (006) reflections toward lower diffraction angles, corresponding to an expansion of the basal spacing from approximately 0.76 to 0.89 nm.[12] This expansion indicates the partial replacement of interlayer CO_3^{2-} by NO_3^-/methanol-containing species and the opening of the interlayer galleries. Meanwhile, the characteristic in-plane LDH framework was retained, suggesting that the solvent-assisted exchange proceeds mainly through a topotactic interlayer modification rather than dissolution–reprecipitation of the host layers.

Taken together, the XRD results demonstrate that the mechanochemical route rapidly generates carbonate-intercalated CoAl-LDH precursors after water washing, while the subsequent methanol–nitric acid treatment expands the interlayer spacing and increases structural accessibility. This structural activation provides the basis for the enhanced fluoride capture behavior discussed in the following sections.

3.2 Solvent- and composition-dependent structural evolution during anion exchange

The solvent-dependent structural evolution of CoAl-LDHs during nitrate exchange was investigated by XRD (Fig. 3). Before exchange, all water-washed samples with different Co/Al feed ratios showed typical reflections of carbonate-intercalated LDHs, including the basal (003) and (006) reflections and the non-basal (110) reflection (Fig. 3a). These results indicate that carbonate-intercalated CoAl-LDHs were successfully formed after mechanochemical synthesis and water washing, regardless of the Co/Al ratio within the investigated range.

After methanol–nitric acid treatment, the (003) and (006) reflections shifted toward lower diffraction angles, confirming the expansion of the interlayer spacing after nitrate/methanol-assisted exchange (Fig. 3b). Meanwhile, the (110) reflection remained nearly unchanged, indicating that the in-plane brucite-like host layers were largely preserved during the exchange process. The basal reflections became broader and weaker with increasing Co/Al ratio, accompanied by an intensified broad hump between 30° and 40°. This suggests that the solvent-assisted exchange mainly affects the interlayer stacking order rather than destroying the host-layer framework.

A similar but less pronounced structural evolution was observed for the ethanol–nitric acid treated samples (Fig. 3c). Compared with MN-LDH, EN-LDH showed weaker low-angle shifted basal reflections and more evident residual LDH

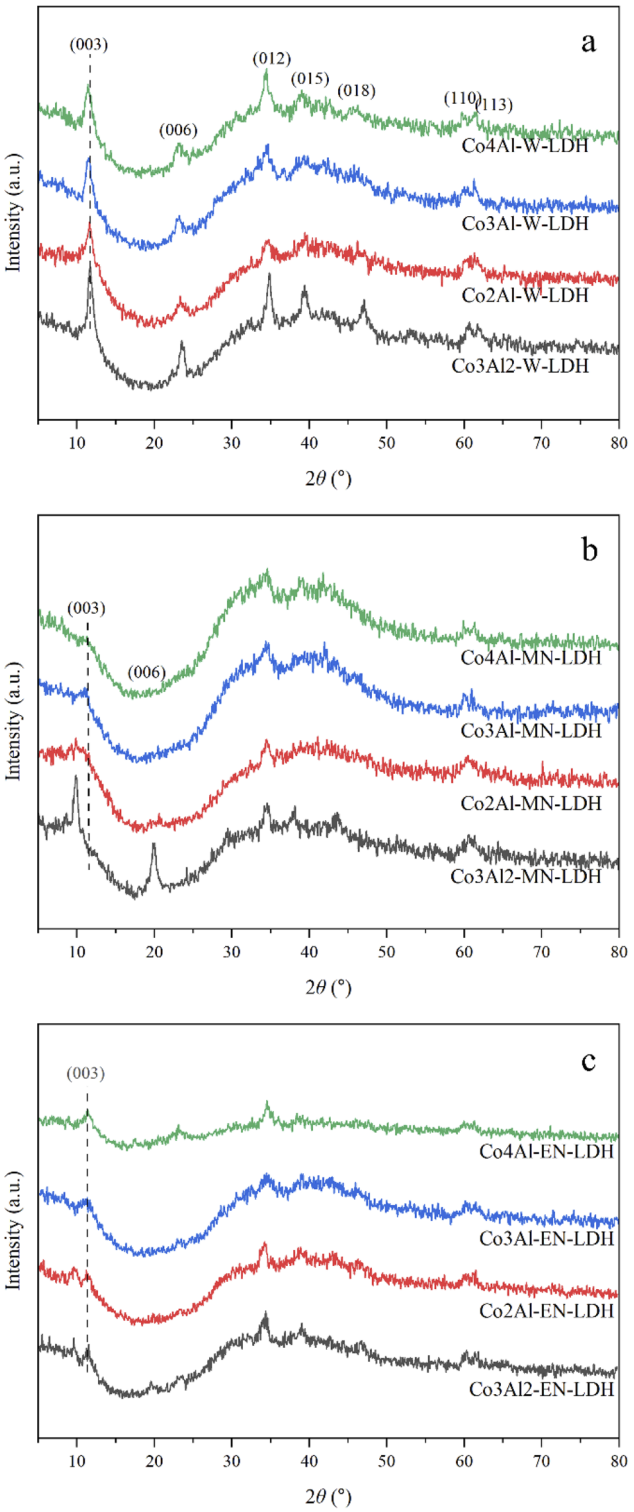

Fig. 3 Comparison of the XRD pattern of samples, (a) after water washing and (b) after subsequent methanol–nitric acid replacement or (c) ethanol–nitric acid replacement at different Co/Al feed ratios.

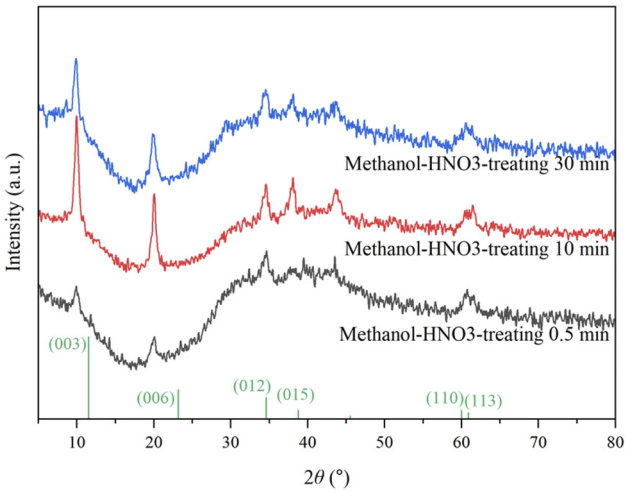

Fig. 4 Effect of methanol–nitric acid treatment time on the XRD pattern of MN-LDH.

reflections at the original positions. These XRD results indicate that methanol and ethanol induce different degrees of interlayer expansion and stacking disorder. Methanol, owing to its smaller molecular size and higher polarity,[20] can more readily penetrate the interlayer galleries and promote rapid expansion and turbostratic disorder, whereas ethanol produces a milder structural response during nitrate exchange. This solvent-dependent behavior is consistent with the Aqueous Miscible Organic Solvent Treatment (AMOST) concept reported by O'Hare and co-workers,[21,22] in which aqueous-miscible organic solvents weaken interlayer interactions and promote disordering or delamination of LDHs.

The time-dependent XRD patterns further reveal the structural evolution of MN-LDH during methanol–nitric acid treatment (Fig. 4). At 0.5 min, the basal (003) reflection was weak and accompanied by a broad hump at 30–40°, indicating an initially disordered interlayer environment. When the treatment time was increased to 10 min, the (003) reflection became sharper and stronger, suggesting improved basal ordering after nitrate/methanol incorporation. Upon further extending the treatment time to 30 min, the relative intensity of the (003) reflection slightly decreased, implying a moderate increase in stacking disorder while the layered framework was still retained. This moderate disorder may improve the accessibility of interlayer sites, which is consistent with the higher fluoride removal efficiency observed for the 30 min-treated sample.

The Co/Al ratio also strongly influenced the structural response to solvent-assisted exchange. As the Co/Al ratio increased from 3 : 2 to 4 : 1, the basal (003) and (006) reflections of MN-LDH gradually broadened, weakened, or even became less discernible, whereas the in-plane (110) reflection remained stable (Fig. 3b). This trend indicates that decreasing the Al^{3+} content mainly reduces the ordering of interlayer stacking, while the brucite-like host layers remain structurally intact. Since Al^{3+} substitution for Co^{2+} generates the positive layer charge of LDHs, the Co_3Al_2 composition possesses the highest layer charge density among the tested samples. This higher layer charge density favors electrostatic attraction toward anionic species and helps maintain a more stable layered structure during solvent-assisted exchange.

Therefore, the superior fluoride adsorption performance of Co_3Al_2-MN-LDH can be associated with the higher nominal Al content and positive layer-charge density. Although a minor contribution from amorphous Al-containing species cannot be completely excluded, the systematic dependence on solvent treatment and Co/Al ratio suggests that layer charge density and interlayer accessibility dominate the observed adsorption enhancement.

3.3 Surface chemistry and interlayer microenvironment evolution

To further elucidate the surface and interlayer microstructures of CoAl-LDHs prepared by the mechanochemical–anion exchange method, FTIR, XPS, and nitrogen adsorption–desorption tests were conducted on Co_3Al_2-LDH samples after water washing, methanol–nitric acid treatment, and ethanol–nitric acid treatment, respectively.

3.3.1 FTIR analysis. The FTIR spectra provide direct evidence for the evolution of the interlayer chemical environment after alcohol-assisted nitrate exchange (Fig. 5 and S1). For W-LDH, the bands at 558 and 616 cm^{-1} are assigned to M–O lattice vibrations of the LDH host layers,[8] while the broad feature at 790–862 cm^{-1} and the bands at 1357 and 1515 cm^{-1} correspond to carbonate species in the interlayer.[23] After methanol–nitric acid or ethanol–nitric acid treatment, new nitrate-related bands appeared at 826–839 cm^{-1} and 1386 cm^{-1}, accompanied by the emergence of the characteristic NO_3^- combination band at 1763 cm^{-1}, confirming successful nitrate incorporation.[14]

Meanwhile, the carbonate-related band at 1515 cm^{-1} became almost indiscernible, although the 1357 cm^{-1} signal remained partially visible in MN-LDH, indicating that carbonate exchange was substantial but not complete. In contrast, the water–nitric acid treated sample (WN-LDH, Fig. S1) retained a spectrum largely similar to that of W-LDH, without the clear alcohol-related features observed for MN-LDH and EN-LDH. The main changes in WN-LDH were the enhanced broad O–H stretching band around 3432 cm^{-1} and the emergence of a broad feature in the 2930–3200 cm^{-1} region, suggesting increased hydration and stronger hydrogen-bonding interactions among interlayer water molecules, anions, and layer hydroxyls.

Weak bands at 2767 and 2735 cm^{-1} can be attributed to alkyl vibrations,[14] supporting the presence of alcohol molecules associated with the interlayer region. The broad O–H stretching band around 3432 cm^{-1} also changed after exchange, suggesting a rearranged hydrogen-bonding network involving layer hydroxyls, interlayer anions, water, and alcohol molecules.[8] Compared with WN-LDH, the alcohol-treated samples therefore show not only nitrate incorporation but also a distinct modification of the interlayer solvation environment.

Overall, the FTIR results demonstrate that alcohol-assisted nitrate treatment does not destroy the LDH host layers but modifies the interlayer anion composition and hydrogen-bonding microenvironment. The WN-LDH reference further confirms that nitric acid treatment in water mainly strengthens hydration and hydrogen-bonding interactions, whereas methanol and ethanol are required to generate the alcohol-associated interlayer microenvironment. Among them, MN-LDH retains partial carbonate but exhibits a more strongly modified interlayer environment, consistent with the solvent-mediated structural activation discussed above.

3.3.2 XPS analysis. XPS was further employed to examine the surface composition and local electronic environment of CoAl-LDHs before and after solvent-assisted exchange (Fig. 6). In the survey spectra, W-LDH exhibited signals of Co, Al, C, N, O, and residual Na. After methanol–nitric acid and ethanol–nitric acid treatment, the Na signal disappeared, indicating that the exchange process also removed residual soluble sodium salts. The surface Co/Al atomic ratios of W-LDH, MN-LDH, and EN-LDH were 1.06, 1.05, and 1.04, respectively, nearly unchanged after treatment. This result indicates that the host-layer metal composition was well preserved and that no significant selective dissolution of Co or Al occurred during solvent-assisted exchange.

The high-resolution C 1s spectra show that W-LDH contains a dominant carbonate-related component near 289.1–289.3 eV, together with the adventitious carbon peak at 284.8 eV and a C–O component at around 286.1 eV.[23–26] After alcohol–nitric acid treatment, the carbonate-related C 1s contribution decreased markedly but did not completely disappear, consistent with the partial retention of carbonate observed by FTIR. Meanwhile, the relative intensity of the C–O component increased, especially for MN-LDH, supporting the presence of alcohol-derived species associated with the interlayer or surface environment.

The Co 2p spectra show a spin–orbit splitting of approximately 16.0 eV between Co $2p_{3/2}$ and Co $2p_{1/2}$, characteristic of high-spin Co^{2+} species. The Al 2p spectra also show no evidence of a new dominant Al-containing phase after exchange. These results confirm that the Co–Al hydroxide host layers remain chemically stable during solvent-assisted treatment. Compared

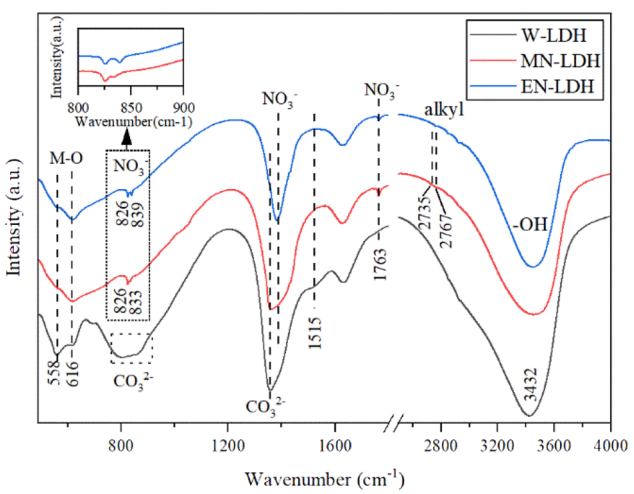

Fig. 5 FTIR comparison of LDH after water washing (W-LDH), after treatment with methanol–nitric acid (MN-LDH) and ethanol–nitric acid (EN-LDH), respectively.

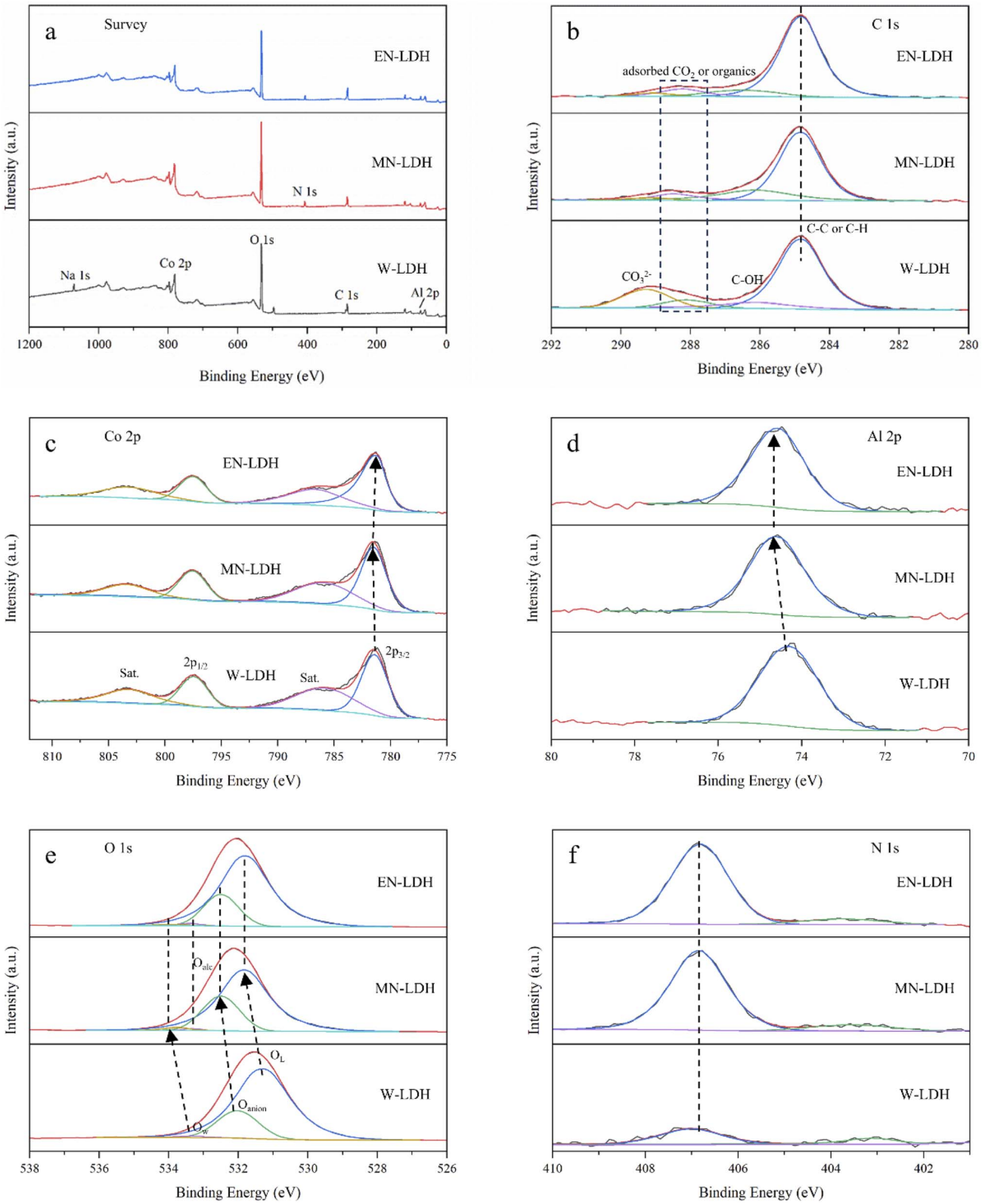

Fig. 6 XPS of LDH after water washing and after treatment with methanol–nitric acid and ethanol–nitric acid, respectively. (a) Full spectrum, (b) C 1s, (c) Co 2p, (d) Al 2p, (e) O 1s, (f) N 1s.

with W-LDH, the Co 2p and Al 2p binding energies changed slightly after alcohol–nitric acid exchange, indicating that the local electronic environment of the metal centers was modified. Such shifts are more reasonably attributed to the weakening and reconstruction of the interlayer hydrogen-bonding network after partial replacement of strongly interacting CO_3^{2-} by NO^{3-}

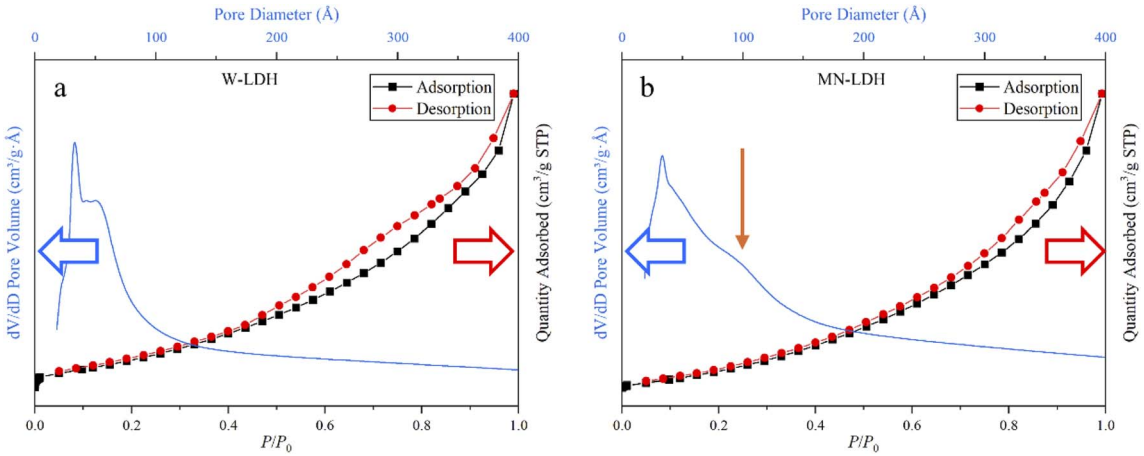

Fig. 7 Comparison of nitrogen adsorption–desorption curves and pore size distributions of (a) W-LDH and (b) MN-LDH.

and alcohol molecules, rather than to a stronger intrinsic interaction between NO^{3-} and the LDH layers. The differing shifts of Co 2p and Al 2p XPS peaks are a predictable consequence of the differing sensitivities of transition metal d-orbitals (Co) and stable main-group closed shells (Al) to the modified interlayer environment.

The O 1s spectra provide further evidence for this interlayer microenvironment change. The fitted O 1s components can be assigned to lattice oxygen bonded to metal ions, oxygen from interlayer anions, adsorbed/interlayer water, and alcohol-related oxygen.[24,26,27] After solvent-assisted exchange, the lattice oxygen component shifted to higher binding energy, while the anion-related component also changed with nitrate incorporation. A weak alcohol-related oxygen contribution appeared in MN-LDH and EN-LDH, in agreement with the alkyl-related FTIR signals. These changes indicate that the exchange process altered the local coordination and hydrogen-bonding environment around layer hydroxyls and interlayer species.

The N 1s spectra show a distinct nitrate-related peak at approximately 406.9 eV after alcohol–nitric acid treatment, confirming the incorporation of NO_3^- into the LDH structure. A weak signal in the 402–405 eV region may be related to minor reduced nitrogen species generated during XPS measurement.[14] The increased nitrate signal after exchange, together with the decreased carbonate contribution in C 1s and the alcohol-related components in C 1s/O 1s, demonstrates that alcohol–nitric acid treatment partially replaces carbonate with nitrate while introducing alcohol-associated interlayer species. Overall, the XPS results confirm that solvent-assisted exchange preserves the Co–Al host-layer framework but substantially modifies the interlayer chemical and electronic microenvironment, consistent with the FTIR and XRD results discussed above. The atomic percentages of elements in various bonding states (by peak fitting) in the sample are given in Table S1.

3.3.3 N_2 adsorption–desorption analysis. The textural properties of W-LDH and MN-LDH were further examined by N_2 adsorption–desorption measurements (Fig. 7). Both samples exhibited typical type IV isotherms with H3-type hysteresis loops, indicating the presence of slit-like mesopores associated with the stacking of plate-like LDH particles.[28] In the low-pressure region (P/P_0 < 0.1), W-LDH and MN-LDH showed similar adsorption behavior, suggesting that the basic micropore/small-mesopore contribution and the intrinsic surface area of the LDH particles were largely retained after methanol–nitric acid treatment. In the high-pressure region (P/P_0 > 0.8), MN-LDH displayed a slightly steeper N_2 uptake than W-LDH, and its pore size distribution became broader, especially in the larger mesopore/macropore range.

The BET specific surface area and total pore volume of the two samples were very close: 197.64 $m^2\ g^{-1}$ and 0.58 $cm^3\ g^{-1}$ for W-LDH, and 194.70 $m^2\ g^{-1}$ and 0.58 $cm^3\ g^{-1}$ for MN-LDH, respectively. These results indicate that the methanol–nitric acid treatment did not create a substantially larger absolute surface area or pore volume. Therefore, the enhanced fluoride adsorption of MN-LDH should not be simply attributed to an increase in BET surface area.

Instead, the higher N_2 uptake of MN-LDH at high relative pressure is more reasonably assigned to enhanced interparticle textural porosity. Because methanol has a lower surface tension than water, the capillary contraction during drying is weakened, which can reduce hard agglomeration of LDH crystallites and generate looser particle packing. Such interparticle voids favor capillary condensation at high relative pressure and lead to a broader pore size distribution. This interpretation is also consistent with the XRD results, where the retained basal reflections indicate that MN-LDH is not completely disordered at the crystallographic level before fluoride adsorption.

Overall, the N_2 adsorption–desorption results show that methanol-mediated activation mainly optimizes the mesoscopic packing and mass-transfer environment rather than increasing the total surface area. Together with the XRD, FTIR, and XPS evidence, these textural changes support the view that the improved fluoride capture performance of MN-LDH arises from enhanced interlayer accessibility, modified interlayer chemistry, and more favorable diffusion pathways, rather than from a simple surface-area effect.

3.3.4 Distinct roles of methanol and ethanol in interlayer exchange and structural activation. Integrating the XRD, FTIR,

and XPS results, the methanol–nitric acid and ethanol–nitric acid systems can be distinguished by their different exchange and structural activation behaviors. In the methanol system, the smaller molecular size and higher polarity of methanol favor rapid penetration into the LDH interlayer galleries. This promotes interlayer expansion and turbostratic disorder, as evidenced by the XRD results, but the rapid and non-equilibrium exchange also leaves part of the original carbonate species retained in the interlayer region, as indicated by FTIR. Accordingly, the local coordination environment in MN-LDH contains coexisting carbonate, nitrate, and methanol-related species, leading to a more heterogeneous surface chemical environment in XPS.

By contrast, ethanol induces a milder and slower interlayer exchange process. The FTIR results show weaker carbonate-related signals and stronger nitrate features in EN-LDH, indicating a more complete carbonate-to-nitrate exchange than that in MN-LDH. The corresponding XPS spectra also suggest a relatively less heterogeneous local chemical environment. However, compared with methanol, ethanol produces a weaker structural activation effect, as reflected by the less pronounced interlayer expansion and different basal reflection evolution in XRD. Therefore, methanol is more effective in promoting structural activation and interlayer accessibility, whereas ethanol favors a more complete chemical exchange. This contrast explains why MN-LDH exhibits a more activated interlayer structure despite retaining minor carbonate residues.

3.4 Evaluation of fluoride adsorption performance

3.4.1 Effect of the Co/Al molar ratio. Fig. 8a compares the fluoride removal efficiencies of CoAl-LDHs synthesized at various Co/Al molar ratios (3 : 2, 2 : 1, 3 : 1, and 4 : 1) before and after methanol–nitric acid exchange. The results indicate that the pristine water-washed samples (W-LDH) exhibited poor performance at an initial concentration of 10 mg L^{-1}, with a maximum removal efficiency of only 24.89%. In contrast, the fluoride uptake of the activated samples (MN-LDH) significantly increased across all ratios. Notably, the 3 : 2 ratio sample achieved a removal efficiency of 94.89%, representing a nearly four-fold enhancement compared to its pristine state. Furthermore, for both the pristine and activated series, the fluoride removal efficiency generally followed a decreasing trend as the Co/Al ratio increased, suggesting that the layer charge density remains a primary determinant of adsorption affinity.

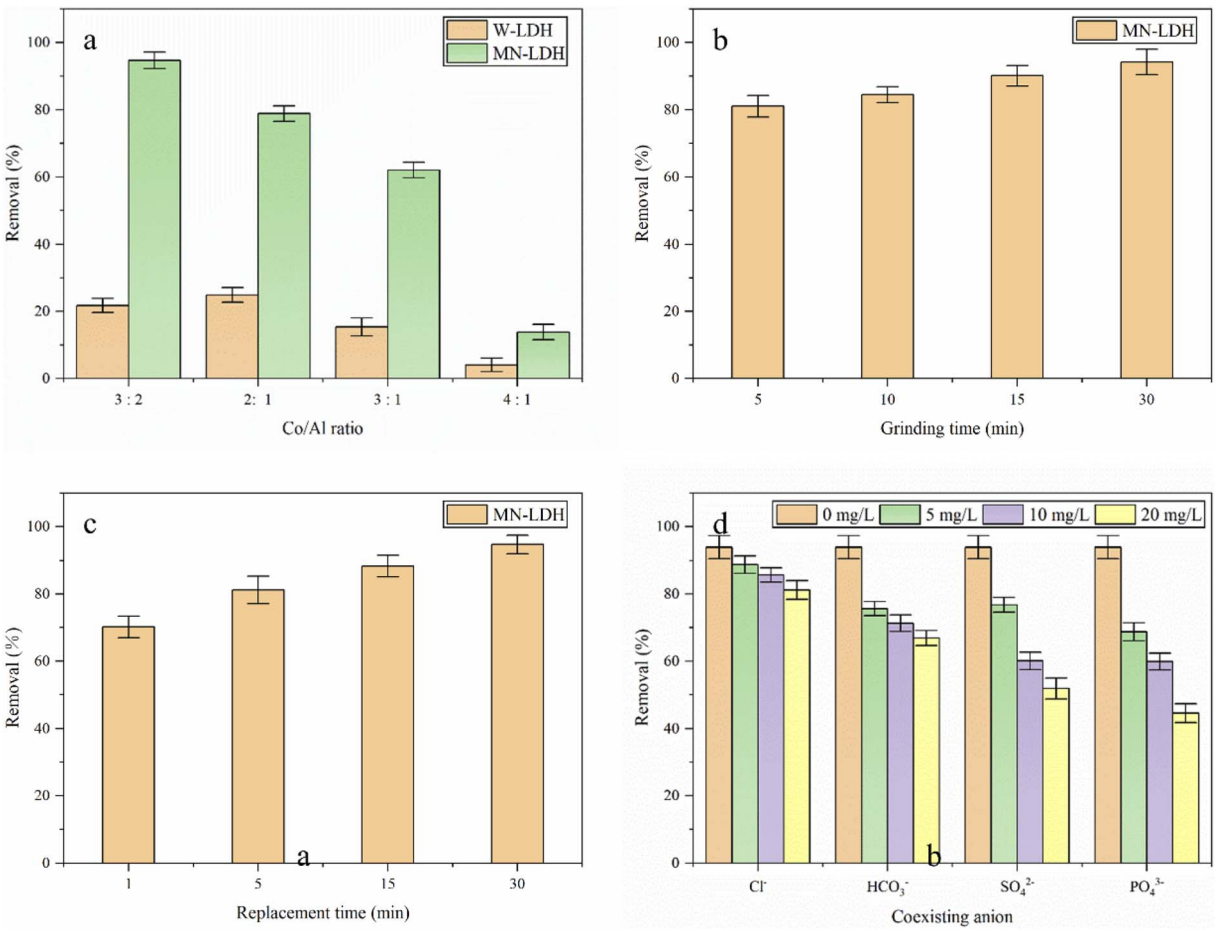

Fig. 8 (a) Comparison of sample performance before and after replacement at different Co/Al feed ratios, and (b) raw material grinding time, (c) methanol–nitric acid replacement time, and (d) effect of coexisting anions on the fluoride removal efficiency of MN-LDH samples.

Consequently, the 3 : 2 ratio was selected for subsequent systematic investigations.

3.4.2 Effect of grinding duration. The influence of mechanochemical grinding time on the fluoride removal efficiency of MN-LDH is shown in Fig. 8b. Even at a short grinding duration of 5 min, the removal efficiency reached 81.09%, and continued to rise as the duration was extended, peaking at 30 min. While XRD results suggested that structural equilibrium is reached within 10 min, the further enhancement in performance with prolonged grinding may stem from the reduction of particle size or the generation of more defect sites along the layer edges. These findings imply that fluoride sequestration depends not only on interlayer ion exchange but also on the spatial accessibility provided by physical turbostratic disorder and morphological refinement. Therefore, a 30 min grinding time was adopted as the baseline for this study.

3.4.3 Effect of methanol–nitric acid exchange time. Fig. 8c illustrates the impact of the methanol–nitric acid treatment duration on fluoride removal. Within just 30 s, the efficiency reached 70.21%. As the exchange time progressed to 5, 15, and 30 min, the removal rates increased to 81.19%, 88.32%, and 94.89%, respectively. The reason for this trend is that with increasing treatment time, methanol-assisted exchange progressively improves interlayer accessibility and promotes partial replacement of carbonate by nitrate/methanol-associated species.

3.4.4 Effect of adsorbent dosage. The effect of adsorbent dosage on fluoride removal performance is presented in Fig. S2. Increasing the dosage from 0.25 g L^{-1} to 0.5 g L^{-1} resulted in a rapid boost in efficiency from 54.41% to 94.89%. This enhancement is primarily attributed to the increased abundance of active sites available for fluoride interaction. However, further increasing the dosage to 0.75 g L^{-1} only yielded a marginal improvement to 96.72%, suggesting that the system approached a saturation limit. Conversely, the equilibrium adsorption capacity (q_e) exhibited a downward trend as the dosage increased; q_e decreased from 21.768 mg g^{-1} at 0.25 g L^{-1} to 18.952 mg g^{-1} at 0.5 g L^{-1}. This phenomenon occurs because, at lower dosages, the high relative concentration of fluoride ions ensures efficient utilization of the active sites, whereas at higher dosages, a relative deficit of fluoride ions leads to the underutilization of the surplus active sites. Accordingly, a dosage of 0.5 g L^{-1} was utilized for the following experiments.

3.4.5 Adsorption selectivity. Fig. 8d depicts the influence of four coexisting anions (Cl^-, HCO_3^-, SO_4^{2-}, PO_4^{3-}) at various concentrations on the fluoride removal efficiency of MN-LDH. Generally, higher concentrations of competing ions led to a more pronounced inhibition of fluoride uptake. The observed interference sequence was: $Cl^- < HCO_3^- < SO_4^{2-} < PO_4^{3-}$. The presence of Cl^- had a less than 15% reduction, owing to its monovalent nature and low charge density, which results in weak electrostatic attraction to the layers. In contrast, PO_4^{3-} exerted the most significant interference. This is primarily because its high trivalent charge density and strong coordination affinity allow it to form robust bonds with the Al centers within the LDH layers, leading to intense competition for active sites.

3.5 Adsorption kinetics and thermodynamics

3.5.1 Adsorption kinetics. Based on the kinetic framework summarized by Wang *et al.*[29] and the multi-model kinetic evaluation strategy (MMKES) proposed in our previous work,[30] the adsorption process generally involves three sequential stages: (i) external diffusion (film diffusion), where the adsorbate traverses the liquid film to reach the adsorbent surface; (ii) internal diffusion (intra-particle diffusion), where the adsorbate migrates within the pores toward the active sites; and (iii) surface adsorption, where the adsorbate is ultimately immobilized at the active sites through physical or chemical interactions.

To discern whether the rate-limiting step resides in the initial transport (diffusion) or the final surface interaction, the Pseudo-First-Order (PFO)[31] and Pseudo-Second-Order (PSO)[32] models were first applied. Subsequently, the Boyd model[33] and the Weber–Morris (W&M) model[34] were introduced to identify the specific rate-controlling step during the initial stages of adsorption. Furthermore, the RSO model,[35] which offers a more defined physical significance, was employed to scrutinize the surface adsorption behavior in the final stage. Finally, the Elovich model[36] was utilized to provide a comprehensive description of the entire adsorption process and to facilitate a comparison of adsorption rates across various experimental conditions.

The mathematical expressions for these models and the fitting results obtained using the such MMKES methodology are summarized in Tables S2 and S3, respectively. The PSO model generally showed better fitting than the PFO model, suggesting that the overall kinetics are more closely associated with surface interaction/fixation than with a simple first-order diffusion-controlled process. Instead, the final surface fixation step, involving electrostatic attraction and hydrogen-bonding interactions, likely plays an important role in controlling the overall adsorption rate (Fig. 9).

In the initial stage, the better agreement with the Boyd model than the W&M model suggests a significant contribution of film diffusion. This result can be attributed to the structural features of the methanol-activated material: the interlayer galleries were partially opened and became more accessible after methanol activation, and under the influence of strong electrostatic attraction, internal diffusion resistance was reduced to some extent. Consequently, the initial adsorption rate is primarily governed by transport through the water film, while the overall rate is ultimately constrained by the final occupancy or seating process at the active sites.

The Elovich model provides the best fit for the entire adsorption kinetics of MN-LDH (Table S3). The adsorption rates of fluoride ions at different concentrations were compared and the results show that the adsorption rate initially increases and then decreases with increasing fluoride ion concentration. The initial increase in adsorption rate (from 5 to 10 mg L^{-1}) is driven by the enhanced concentration gradient, which overcomes the boundary layer resistance identified by the Boyd model. However, the subsequent rate decline at higher concentrations (>10 mg L^{-1}) may reflect site saturation and increased

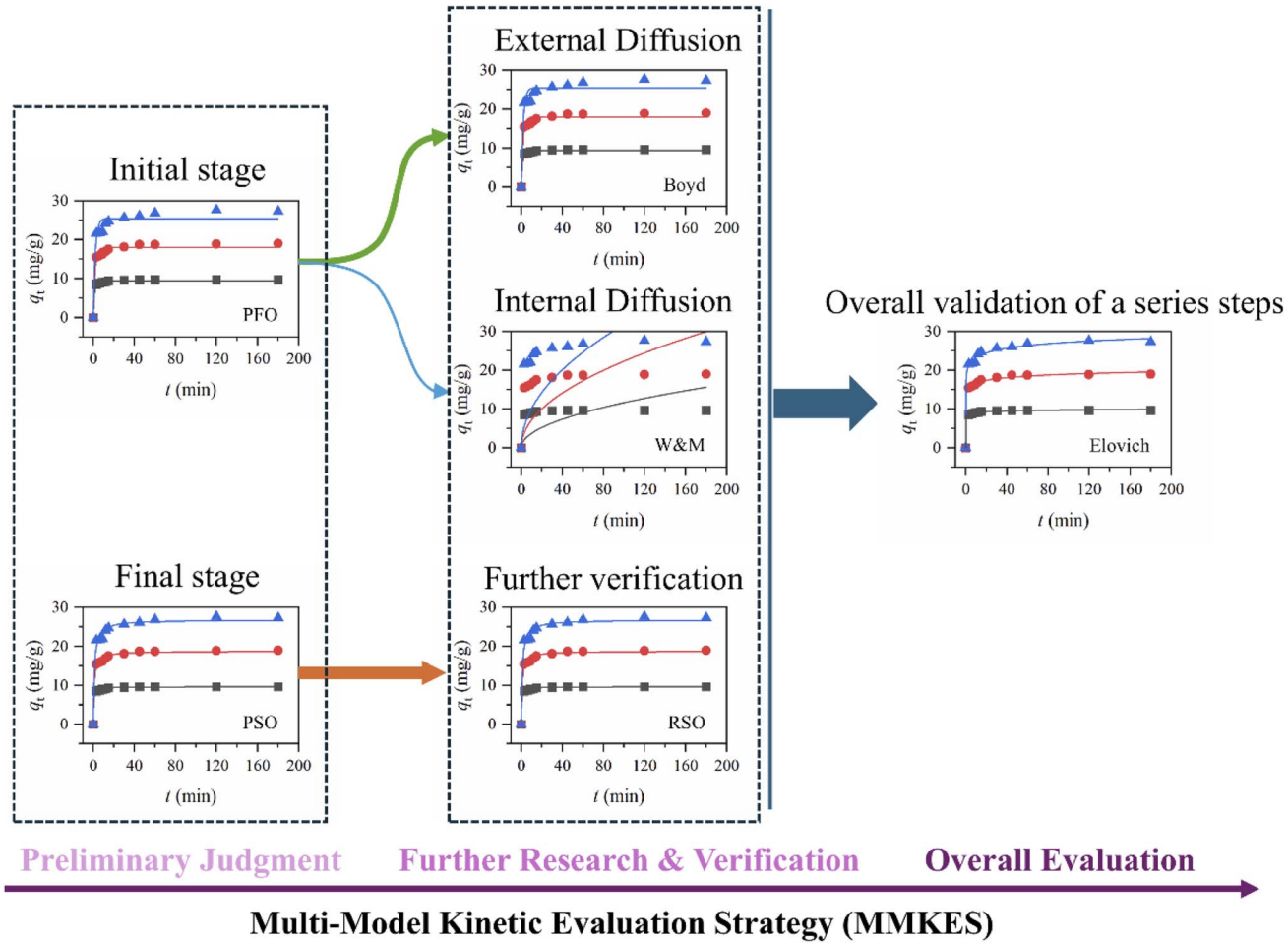

Fig. 9 Adsorption kinetics analysis of MN-LDH by MMKES (initial F^- concentration = 10 mg L^{-1}; adsorbent dosage = 0.5 g L^{-1}; initial pH = 7.0; T = 298 K).

resistance for further fluoride uptake at higher surface coverage. Rapid occupancy of surface active sites by F^- ions may be related to partial interlayer rearrangement and electrostatic screening after fluoride uptake, consistent with the post-adsorption FTIR and XPS results. This may increase the resistance for further fluoride uptake at high surface coverage.

Interestingly, the Elovich parameter β exhibited a downward trend with increasing initial fluoride concentration, suggesting a reduction in surface coverage resistance at higher initial fluoride concentrations. This trend may arise from the combined effects of a stronger concentration gradient and easier replacement of weakly bound interlayer solvent molecules. The post-adsorption FTIR and XPS results confirm that methanol-related species can be displaced during fluoride uptake. The concentration-dependent kinetic trend may therefore be related to easier replacement of weakly bound interlayer solvent species at higher driving force.

3.5.2 Adsorption isotherms and thermodynamic analysis. The fluoride adsorption isotherms of MN-LDH at 303, 313, and 323 K were fitted using the non-linear Langmuir[37] and Freundlich[38] models (Fig. S3 and Table S4). Overall, the Freundlich model provided better fitting than the Langmuir model, as reflected by the higher correlation coefficients in Table S4. This result is consistent with the structural and surface heterogeneity suggested by XRD and XPS: the methanol-induced turbostratic activation likely produces energetically heterogeneous adsorption environments.

The Langmuir separation factor R_L was between 0 and 1 under all tested conditions, indicating favorable fluoride adsorption (Table 1).[39] Furthermore, the decrease in R_L with increasing initial fluoride concentration indicates that adsorption remains favorable over the examined concentration range. The slightly lower R_L values at lower temperature are consistent with the exothermic character discussed below.

To further quantify the energetic changes, the standard thermodynamic parameters were calculated by eqn (3)–(5):

Table 1 Separation factor R_L of the Langmuir isotherm at initial fluoride concentrations 5–100 mg L^{-1}

C_0		5	10	20	50	100
$R_L = \frac{1}{1+K_L C_0}$	303 K	0.24624	0.14041	0.0755	0.03163	0.01607
	313 K	0.25652	0.14713	0.07941	0.03335	0.01696
	323 K	0.2666	0.1538	0.08331	0.03508	0.01785

Table 2 Apparent thermodynamic parameters of fluoride adsorption onto MN-LDH

T (K)	$\ln K_0$	ΔG^0 (kJ mol^{-1})	ΔH^0 (kJ mol^{-1})	ΔS^0 (kJ mol^{-1} K^{-1})
303 K	6.417	−16.166	−4.346	0.039
313 K	6.362	−16.557		
323 K	6.310	−16.946		

$$K_0 = K_L \times C_{std} \quad (3)$$

$$\Delta G^0 = -RT \ln K_0 \quad (4)$$

$$\ln K_0 = \frac{\Delta S^0}{R} - \frac{\Delta H^0}{RT} \quad (5)$$

where C_{std} is the standard concentration (1000 mg L^{-1}); K_L is the Langmuir constant; K_0 was the equilibrium constant obtained by converting K_L to a dimensionless form using the standard concentration C_{std}. ΔG^0, ΔS^0, ΔH^0 represent the standard Gibbs free energy, entropy, and enthalpy changes, respectively; R is the universal gas constant, and T is the absolute temperature. Although Langmuir fitting was not superior to Freundlich, K_L was used only to obtain an apparent equilibrium constant for comparative thermodynamic estimation; therefore, the thermodynamic parameters should be interpreted as apparent values.

The negative ΔG^0 values indicate that fluoride adsorption onto MN-LDH is thermodynamically favorable (Table 2). This agrees with the Freundlich parameter $1/n < 1$, which also suggests favorable adsorption behavior (Table S4). Interestingly, ΔG^0 becomes more negative as the temperature increases, suggesting that elevated temperatures actually enhance the spontaneity of the reaction. The negative ΔH^0 value (−4.346 kJ mol^{-1}) indicates a mildly exothermic adsorption process, which may involve favorable electrostatic interactions and hydrogen-bonding contributions. Concurrently, the standard entropy change (ΔS^0) was found to be 0.039 kJ (mol K)$^{-1}$. The positive ΔS^0 value suggests increased disorder at the solid–liquid interface during fluoride uptake.

The thermodynamic results reveal that the fluoride capture by MN-LDH is thermodynamically favored by both a mild exothermic contribution and a positive entropy contribution, with the entropy term playing a major role in the temperature dependence of ΔG^0. The exothermic nature ($\Delta H^0 < 0$) typically suggests a decrease in spontaneity with rising temperature, the significant entropy gain ($\Delta S^0 > 0$) further enhances the spontaneity of adsorption at elevated temperature. Specifically, this entropy gain may arise from the release of confined or weakly bound methanol/water molecules during fluoride uptake. This transition from a highly restricted state to a free state produces a substantial increase in the system's total entropy, suggesting that solvent exclusion contributes importantly to the thermodynamic driving force. These thermodynamic results are consistent with the proposed solvent-exclusion-assisted fluoride capture mechanism. The structural origin of this behavior is further supported by post-adsorption characterization.

3.6 Benchmark comparison with reported fluoride adsorbents

To evaluate the competitive position of the methanol-activated MN-LDH, its Langmuir maximum adsorption capacity (q_m) was compared with reported fluoride adsorbents under reported initial near-neutral conditions (Table S5). Because most literature reports provide only the initial pH rather than the equilibrium pH, Table S5 lists the reported equilibrium pH where available and marks unavailable values as NR; the initial pH values are retained as reference conditions. Under an initial pH of 7.0, MN-LDH exhibited a q_m of 58.78 mg g^{-1}, which is among the higher values reported under comparable near-neutral conditions. This value is higher than several recently reported adsorbents, such as citrate-stabilized amorphous calcium phosphate (30.99 mg g^{-1}, 2025),[40] MgO-modified sucrose-derived porous carbon (26.6 mg g^{-1}, 2024).[41] Notably, the q_m of MN-LDH under the reported conditions even exceeds that of established high-capacity inorganic candidates like La^{3+}-exchanged zeolite (51.5 mg g^{-1})[42] and Fe–Al–Ce trimetal hydroxide (51.3 mg g^{-1}).[43] More importantly, this performance was achieved at a relatively low adsorbent dosage of 0.5 g L^{-1}, suggesting efficient utilization of accessible adsorption sites under the tested low-dosage condition.

It should be noted that a fully strict comparison based on equilibrium pH is limited by incomplete reporting in the literature. Nevertheless, the available data show that MN-LDH exhibits competitive fluoride uptake under near-neutral conditions, together with rapid adsorption kinetics and structural stability, supporting its potential for neutral fluoride-containing aqueous systems.

3.7 Adsorption mechanism

3.7.1 XRD, FTIR, and XPS analysis of post-adsorption MNF-LDH. The structural and chemical changes of MN-LDH after fluoride adsorption were examined by XRD, FTIR, and XPS. In the XRD pattern of MNF-LDH, the basal (003) reflection became weaker and evolved into a broad feature between 9.9° and 12.6°, corresponding to a d-spacing range of approximately 7.0–8.9 Å (Fig. 10a). This range overlaps with the typical basal spacings associated with nitrate-, carbonate-, and fluoride-containing LDH interlayers, suggesting that fluoride uptake occurs in a mixed interlayer environment where residual nitrate and carbonate species are still present. Meanwhile, the in-plane (110) reflection remained essentially unchanged, indicating that the brucite-like host layers were largely preserved after fluoride adsorption. A new sharp peak appeared at 50.16°. Considering the absence of simultaneous sharpening of other LDH reflections, this peak is unlikely to originate from a newly ordered F-type LDH phase. It is tentatively associated with a minor fluoride-induced Al–F/OH-containing local domain; further structural evidence would be required for definitive phase assignment.

The FTIR spectra provide further evidence for the exchange of interlayer species during fluoride uptake (Fig. 10b). After adsorption, the nitrate-related bands at 1386 and 1763 cm^{-1} were markedly weakened, indicating that a considerable

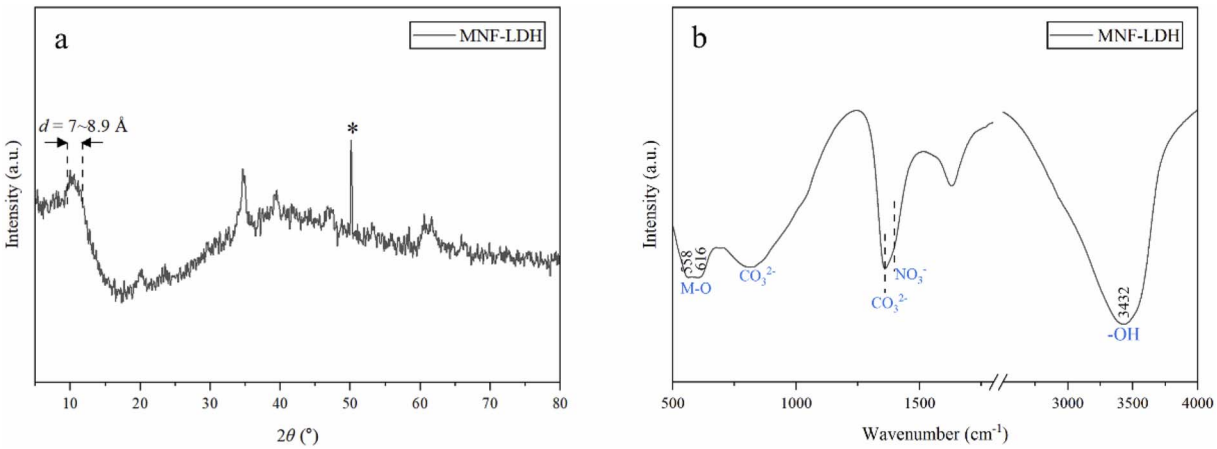

Fig. 10 (a) XRD and (b) FTIR of MN-LDH after fluoride ion adsorption. The asterisk mark in XRD pattern associated with a fluoride-related local crystalline phase formed after adsorption.

fraction of nitrate species was displaced during fluoride capture. The methanol-related weak bands at 2767 and 2735 cm^{-1} also nearly disappeared after adsorption, suggesting that alcohol molecules associated with the interlayer environment were largely removed. These changes are consistent with the replacement of weakly bound nitrate/methanol-containing species by fluoride ions. The retained carbonate-related signal indicates that fluoride adsorption does not involve complete removal of all pre-existing interlayer anions, but rather proceeds through partial anion exchange and interlayer rearrangement.

XPS analysis directly confirms the presence of surface/near-surface fluoride species; together with XRD and FTIR changes, this supports fluoride incorporation into the activated interlayer environment. A distinct F 1s signal appeared at 684.76 eV in MNF-LDH (Fig. 11 and S4), which is consistent with ionic or coordinated fluoride species. In parallel, the N 1s/Al 2p ratio decreased from 0.35 before adsorption to 0.05 after adsorption, while the O_{anion}/O_L ratio in the O 1 s spectrum decreased from 0.37 to 0.05. These changes agree with the FTIR results and indicate substantial replacement or removal of nitrate-related interlayer species during fluoride uptake. The C–O contribution in the C 1s spectrum also decreased from 0.29 to 0.15 relative to the 284.8 eV peak, and the alcohol-related oxygen component in the O 1s spectrum became much weaker, further supporting the exclusion of methanol-related species from the interlayer environment.

After fluoride adsorption, the Al 2p peak shifted from 74.57 to 74.41 eV, and the Co 2p peak shifted from 781.49 to 781.36 eV. The O_L component in the O 1s spectrum also shifted slightly from 531.80 to 531.68 eV. These small negative shifts indicate that fluoride uptake modifies the local electronic environment of the metal hydroxide layers. Rather than implying the formation of a strongly covalent metal–fluoride phase, these shifts more reasonably reflect electronic compensation and local coordination adjustment after fluoride binding and solvent/anion rearrangement. Importantly, the Co/Al atomic ratio remained close to unity after adsorption, suggesting no obvious selective loss of Co or Al from the near-surface region.

To further confirm the structural stability of the material and rule out macroscopic layer dissolution during the adsorption process, the post-adsorption aqueous solution was analyzed using ICP-OES. The measured leached concentrations of Co and Al were merely 0.035 mg L^{-1} and 0.012 mg L^{-1}, respectively. These values are virtually negligible and significantly lower than the stringent discharge thresholds specified in European industrial wastewater standards (0.1 mg L^{-1} for Co and 1.0 mg L^{-1} for Al). This minimized metal leaching is fundamentally governed by the near-neutral pH environment (pH ≈ 7.0) during adsorption, which mitigates aggressive acid attack on the brucite-like layers, as well as the thorough elimination of unreacted metal precursors during the sequential washing steps. These macroscopic leaching results support the structural stability under the tested near-neutral conditions.

Overall, the post-adsorption characterization shows that fluoride capture by MN-LDH involves three coupled processes: partial replacement of nitrate-containing interlayer species, exclusion of methanol-related species, and local electronic adjustment of the Co–Al hydroxide layers. The preservation of the (110) reflection and the stable Co/Al ratio demonstrate that the host-layer framework remains intact, while the weakened basal ordering and spectroscopic changes indicate substantial interlayer rearrangement. These results support a fluoride adsorption mechanism based on anion exchange and solvent-exclusion-assisted interlayer reorganization rather than dissolution–reprecipitation of the LDH framework.

3.7.2 Fluoride capture mechanism. Based on the structural evolution, surface chemical analysis, textural characterization, adsorption kinetics, and thermodynamic results, a methanol-mediated turbostratic activation and solvent-exclusion-assisted fluoride capture mechanism is proposed (Fig. 12). This mechanism can be divided into three successive but closely related stages.

In the first stage, the water-washed W-LDH remains in a carbonate-dominated state. XRD and FTIR results show that

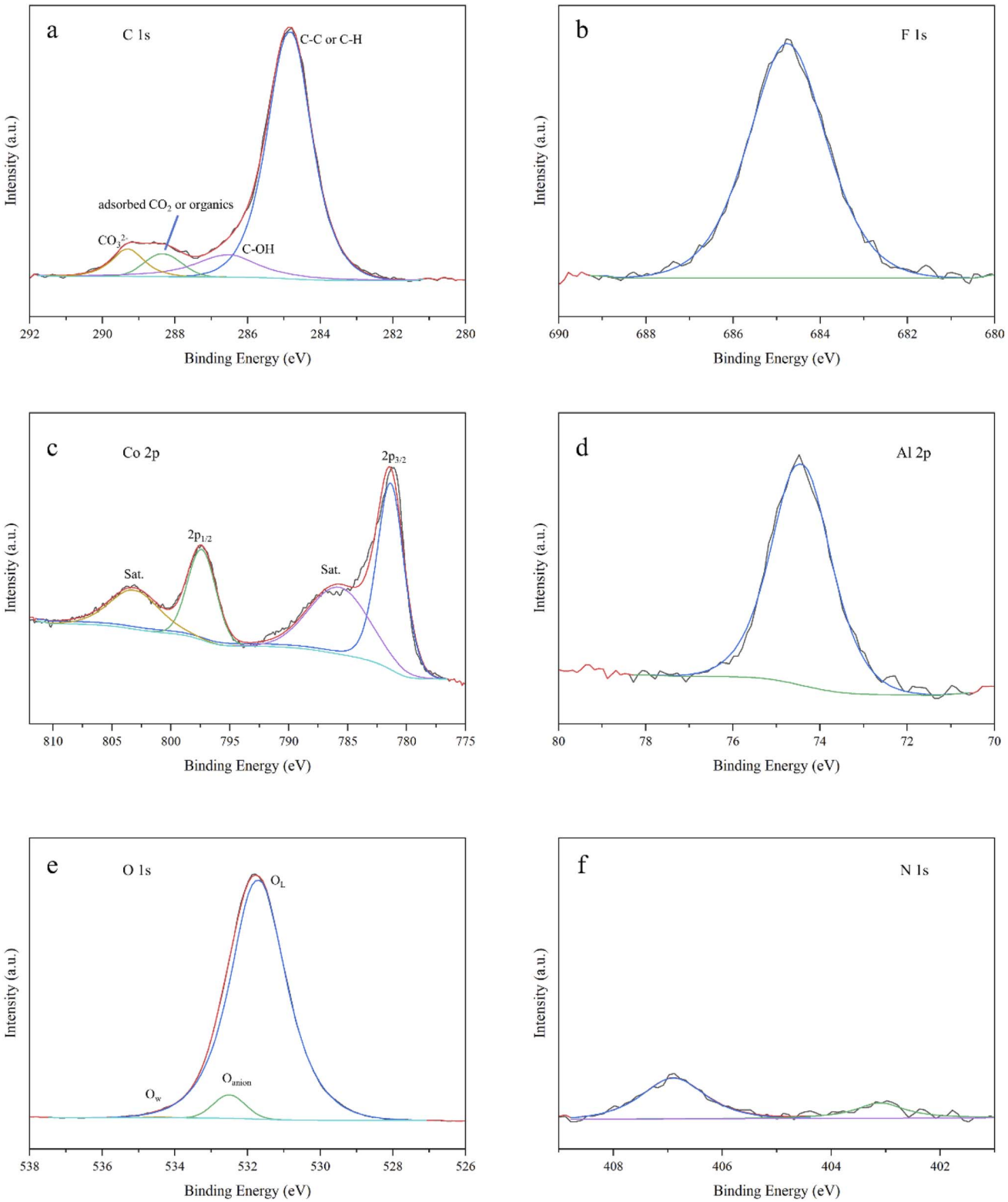

Fig. 11 XPS of MNF-LDH: (a) Full spectrum, (b) C 1s, (c) Co 2p, (d) Al 2p, (e) O 1s, (f) N 1s.

carbonate species occupy the interlayer region and maintain relatively ordered basal stacking. Because CO_3^{2-} interacts strongly with the positively charged LDH layers, the interlayer galleries are compact and less accessible to external fluoride ions. As a result, only limited fluoride uptake is achieved for W-LDH under neutral conditions, indicating that most interlayer adsorption sites are not effectively available in the carbonate-locked precursor.

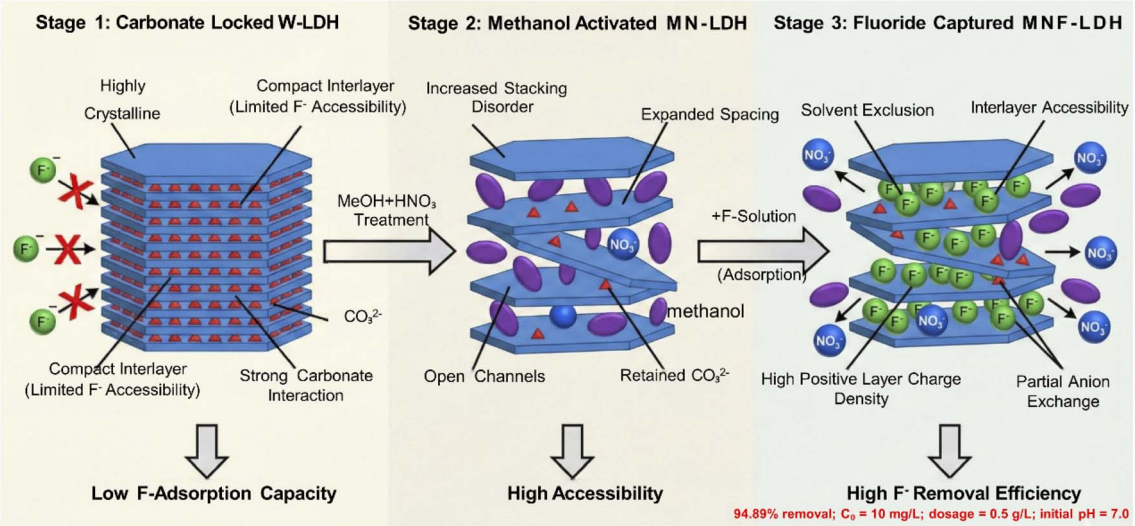

Fig. 12 Schematic illustration of methanol-assisted interlayer activation and solvent-exclusion-assisted fluoride capture by CoAl-LDHs.

In the second stage, methanol–nitric acid treatment activates the interlayer structure of CoAl-LDH. The XRD results show an expansion of the basal spacing and an increase in stacking disorder, while the preserved (110) reflection and stable Co/Al ratio indicate that the brucite-like host layers remain intact. FTIR and XPS analyses further confirm the partial replacement of interlayer carbonate by nitrate species and the introduction of methanol-associated species into the interlayer environment. Therefore, methanol treatment does not simply increase the external surface area; rather, it modifies the interlayer chemistry and improves the accessibility of charged sites. In this activated state, nitrate and methanol-related species are more weakly retained than carbonate, making the interlayer environment more responsive to fluoride exchange.

In the third stage, fluoride adsorption occurs when MN-LDH is exposed to fluoride-containing solution. Fluoride ions can access the activated interlayer region and interact with positively charged metal hydroxide layers through electrostatic attraction, hydrogen bonding, and ligand/anion-exchange interactions. The post-adsorption FTIR spectra show a marked weakening of nitrate-related bands and the near disappearance of methanol-related alkyl vibrations, while XPS reveals the appearance of F 1s signals and a decrease in nitrate- and alcohol-related components. These results indicate that fluoride uptake is accompanied by partial replacement of nitrate species and exclusion of methanol-related species from the interlayer environment. The positive entropy contribution obtained from thermodynamic analysis is consistent with the release of confined or weakly bound solvent molecules during this process.

The structural and chemical evidence also indicates that fluoride capture proceeds without destroying the LDH host framework. After adsorption, the (110) reflection remains nearly unchanged and the Co/Al atomic ratio is retained, suggesting that the Co–Al hydroxide layers act as a stable structural scaffold. Meanwhile, the weakened basal ordering, the reduced nitrate/methanol signals, and the shifts in Co 2p, Al 2p, and O 1s binding energies suggest interlayer rearrangement and local electronic adjustment after fluoride binding. Therefore, the enhanced fluoride removal by MN-LDH originates from the combined effects of high positive layer charge density, methanol-induced interlayer accessibility, partial anion exchange, and solvent-exclusion-assisted rearrangement, rather than from dissolution–reprecipitation or a simple surface-area effect.

4 Conclusion

This study reports a methanol–nitric acid activation strategy for improving the fluoride capture performance of mechanochemically synthesized CoAl-LDHs. Under neutral conditions with an initial fluoride concentration of 10 mg L^{-1}, an adsorbent dosage of 0.5 g L^{-1}, and an initial pH of 7.0, the optimized Co_3Al_2-MN-LDH achieved a fluoride removal efficiency of 94.89%, nearly four times higher than that of the pristine water-washed W-LDH. The Langmuir maximum adsorption capacity reached 58.78 mg g^{-1}, indicating competitive fluoride uptake under near-neutral conditions.

Structural and spectroscopic analyses show that methanol–nitric acid treatment expands the LDH interlayer spacing, increases turbostratic disorder, and modifies the interlayer chemical environment while largely preserving the Co–Al hydroxide host layers. The stable Co/Al ratio and the retained (110) reflection indicate that the activation process proceeds mainly through interlayer modification rather than dissolution–reprecipitation of the LDH framework. FTIR and XPS results further confirm partial replacement of carbonate by nitrate species and the incorporation of methanol-related species into the interlayer environment. Compared with ethanol-assisted treatment, methanol provides stronger structural activation and improved interlayer accessibility, although minor residual carbonate species remain.

Fluoride adsorption by MN-LDH involves partial anion exchange, exclusion of methanol-related interlayer species, aof the metal hydroxide layers. Post-adsorption FTIR and XPS analyses show weakened nitrate- and methanol-related signals together with the appearance of F 1s signals, supporting fluoride incorporation into the activated interlayer environment. Kinetic analysis indicates that fluoride uptake is better described by the pseudo-second-order model, with film diffusion contributing to the initial stage, while thermodynamic analysis suggests a favorable adsorption process with a positive entropy contribution. Overall, the enhanced fluoride capture of MN-LDH arises from the combined effects of high positive layer charge density, methanol-induced interlayer accessibility, and solvent-exclusion-assisted interlayer rearrangement. These findings provide a useful strategy for regulating mechanochemical LDHs toward fluoride removal from neutral fluoride-containing aqueous systems, particularly in industrial wastewater contexts where solvent-assisted material preparation can be appropriately controlled.

Author contributions

Chaoyao Yao: investigation, data curation, validation. Jinan Niu: conceptualization, methodology, writing – original draft, project administration. Mingge Zhi: formal analysis, visualization. Ruixuan Zhang: formal analysis, visualization. Shunle Zhou: formal analysis, visualization. Sonehra Anjum: formal analysis. Fangfang Liu: formal analysis, visualization. Arianit A. Reka: writing – review and editing. Farid Akhtar: writing – review and editing. Peizhong Feng: funding acquisition, resources. Hermenegildo Garcia: supervision, writing – review and editing.

Conflicts of interest

There are no conflicts to declare.

Data availability

Data are available upon request to the corresponding authors.

Supplementary information (SI): additional FTIR and XPS spectra, the effect of adsorbent dosage, adsorption isotherm fitting, XPS-derived elemental compositions, kinetic model equations and fitting parameters, thermodynamic fitting parameters, and comparison of fluoride adsorption performance with reported adsorbents. See DOI: https://doi.org/10.1039/d6ta05412a.

Acknowledgements

The work was financially supported by the National Natural Science Foundation of China (No. 52020105011). Funding by the Spanish Agencia Estatal de Investigación (CEX-2021-001230-S and PID2024-161014 NB-I00 funded by MCIN/AEI/10.13039/501100011033) and the Generalitat Valenciana (CIPROM/2024/071) is also gratefully acknowledged.

References

1 M. Amini, K. Mueller, K. C. Abbaspour, T. Rosenberg, M. Afyuni, K. N. Moller, M. Sarr and C. A. Johnson, *Environ. Sci. Technol.*, 2008, **42**, 3662–3668.
2 W. H. Organization, *Guidelines for Drinking-Water Quality: Incorporating the First and Second Addenda*, World Health Organization, 2022.
3 A. Bhatnagar, E. Kumar and M. Sillanpää, *Chem. Eng. J.*, 2011, **171**, 811–840.
4 K.-H. Goh, T.-T. Lim and Z. Dong, *Water Res.*, 2008, **42**, 1343–1368.
5 Y. Luo, L. Sun, J. Niu, M. Zhi, C. Yao, H. Liu, F. Liu, A. A. Reka, F. Akhtar and P. Feng, *Mater. Lett.*, 2025, **400**, 139118.
6 J. Xie, C. Li, J. Niu, S. Zhang, X. Ou, P. Feng and H. Garcia, *Mater. Lett.*, 2021, **290**, 129517.
7 L. Sun, J. Niu, H. Liu, F. Liu, A. A. Reka, J. Matusik and P. Feng, *RSC Sustainability*, 2025, **3**, 715–737.
8 F. Cavani, F. Trifirò and A. Vaccari, *Catal. Today*, 1991, **11**, 173–301.
9 L. Lv, J. He, M. Wei, D. Evans and X. Duan, *J. Hazard. Mater.*, 2006, **133**, 119–128.
10 S. Tezuka, R. Chitrakar, A. Sonoda, K. Ooi and T. Tomida, *Green Chem.*, 2004, **6**, 104–109.
11 Q. Wang and D. O'Hare, *Chem. Rev.*, 2012, **112**, 4124–4155.
12 N. Iyi, T. Matsumoto, Y. Kaneko and K. Kitamura, *Chem. Mater.*, 2004, **16**, 2926–2932.
13 U. Costantino, F. Marmottini, M. Nocchetti and R. Vivani, *Eur. J. Inorg. Chem.*, 1998, **1998**, 1439–1446.
14 N. Iyi, H. Yamada and T. Sasaki, *Appl. Clay Sci.*, 2011, **54**, 132–137.
15 J. A. Bhojaraj, M. R. Kolinjavadi and M. Rajamathi, *ACS Omega*, 2019, **4**, 20072–20079.
16 R. Ma, Z. Liu, L. Li, N. Iyi and T. Sasaki, *J. Mater. Chem.*, 2006, **16**, 3809–3813.
17 P. Baláž, in *Mechanochemistry in Nanoscience and Minerals Engineering*, Springer, 2008, pp. 257–296.
18 V. Šepelák, A. Düvel, M. Wilkening, K.-D. Becker and P. Heitjans, *Chem. Soc. Rev.*, 2013, **42**, 7507–7520.
19 A. Radha, P. V. Kamath and C. Shivakumara, *Struct. Sci.*, 2007, **63**, 243–250.
20 C. Wohlfarth, *CRC Handbook of Chemistry and Physics*, 1994, vol. 6.
21 Q. Wang and D. O'Hare, *Chem. Commun.*, 2013, **49**, 6301–6303.
22 W. Qiang and D. O'Hare, *Chem. Rev.*, 2012, **112**, 4124–4155.
23 J. T. Kloprogge and R. L. Frost, *J. Solid State Chem.*, 1999, **146**, 506–515.
24 J. F. Moulder, W. Stickle, P. Sobol and K. Bomben, *Handbook of X-ray Photoelectron Spectroscopy*, ed. J. Chastain, Perkin-Elmer Corporation, Physical Electronics Division, Eden Prairie, MN, USA, 1992.
25 G. Beamson and D. Briggs, *High Resolution XPS of Organic Polymers: The Scienta ESCA300 Database*, John Wiley & Sons, Chichester, 1992.

26 M. C. Biesinger, B. P. Payne, A. P. Grosvenor, L. W. Lau, A. R. Gerson and R. S. C. Smart, *Appl. Surf. Sci.*, 2011, **257**, 2717–2730.
27 J. T. Kloprogge, *Appl. Sci.*, 2025, **15**, 1318.
28 M. Thommes, K. Kaneko, A. V. Neimark, J. P. Olivier, F. Rodriguez-Reinoso, J. Rouquerol and K. S. Sing, *Pure Appl. Chem.*, 2015, **87**, 1051–1069.
29 J. Wang and X. Guo, *J. Hazard. Mater.*, 2020, **390**, 122156.
30 H. Liu, L. Sun, J. Niu, Y. Luo, M. Zhi, C. Yao, F. Liu, A. A. Reka, J. Matusik and F. Akhtar, *J. Environ. Chem. Eng.*, 2025, 117083.
31 Q. Hu, Q. Wang, C. Feng, Z. Zhang, Z. Lei and K. Shimizu, *J. Mol. Liq.*, 2018, **254**, 20–25.
32 Y. Ho and G. McKay, *Water Res.*, 1999, **33**, 578–584.
33 G. Boyd, A. Adamson and L. Myers Jr, *J. Am. Chem. Soc.*, 1947, **69**, 2836–2848.
34 G. I. Danmaliki and T. A. Saleh, *J. Cleaner Prod.*, 2016, **117**, 50–55.
35 A. Ritchie, *J. Chem. Soc., Faraday Trans. 1*, 1977, **73**, 1650–1653.
36 S. Y. Elovich and O. Larionov, *Bull. Acad. Sci. USSR, Div. Chem. Sci.*, 1962, **11**, 198–203.
37 Z. Zaheer, A.-A. Aisha and E. S. Aazam, *J. Mol. Liq.*, 2019, **283**, 287–298.
38 X. Guo and J. Wang, *Environ. Pollut.*, 2019, **250**, 737–745.
39 T. W. Weber and R. K. Chakravorti, *AIChE J.*, 1974, **20**, 228–238.
40 R. Su, M. Wang, Y. Jiang, S. Zhang and J. Tan, *Nanomaterials*, 2025, **15**, 621.
41 Y. Li, Y. Xiao, T. Lu, G. He, Z. Ding, D. Wang, P. Zhang and Y. Hu, *Desalin. Water Treat.*, 2024, **319**, 100529.
42 M. S. Onyango, Y. Kojima, O. Aoyi, E. C. Bernardo and H. Matsuda, *J. Colloid Interface Sci.*, 2004, **279**, 341–350.
43 B. Zhao, Y. Zhang, X. Dou, X. Wu and M. Yang, *Chem. Eng. J.*, 2012, **185**, 211–218.

